A Multi-Layer Stacked Microfluidic Tactile Display With High Spatial Resolution

Boxue Shan, Congying Liu, Yuan Guo, Yiheng Wang, Weidong Guo, Yuru Zhang, *Senior Member, IEEE*, and Dangxiao Wang, *Senior Member, IEEE*

***Abstract*—Pneumatic tactile displays dynamically customize surface morphological features with reconfigurable arrays of independently addressable actuators. However, their ability to render detailed tactile patterns or fine textures is limited by the low spatial resolution. For pneumatic tactile displays, the high-density integration of pneumatic actuators within a small space (fingertip) poses a significant challenge in terms of pneumatic circuit wiring. In contrast to the structure with a single-layer layout of pipes, we propose a multi-layered stacked microfluidic pipe structure that allows for a higher density of actuators and retains their independent actuation capabilities. Based on the proposed structure, we developed a soft microfluidic tactile display with a spatial resolution of 1.25 mm. The device consists of a 5 $\times$ 5 array of independently addressable microactuators, driven by pneumatic pressure, each of which enables independent actuation of the surface film and continuous control of the height. At a relative pressure of 1000 mbar, the actuator produced a perceptible out-of-plane deformation of 0.145 mm and a force of 17.7 mN. User studies showed that subjects can easily distinguish eight tactile patterns with 96% accuracy.**

***Index Terms*—High spatial resolution, microfluidic actuator array, multi-layer stacked, tactile display.**

I. Introduction

TOUCH is an essential way for humans to interact with the physical world [1]. By actively touching the micro-3D structure of objects' surfaces, humans are able to perform a wide variety of manipulation tasks in real life, such as reading braille books, discerning fabric patterns, and appreciating sculptures [2]. As a typical tactile interaction device, tactile displays based on morphological changes reproduce the surface features of objects through an integrated array of programmable actuators. In recent years, they have gradually permeated various fields, including Braille display, touchscreen interaction, and virtual reality [3], [4], [5], [6], [7], [8].

In order to present detailed tactile patterns or fine textures, the resolution of the tactile displays needs to be sufficiently high. As reported in [9], [10], the spacing between adjacent contact points of a tactile display has an important impact on human tactile perception performance, and the ideal spatial resolution should be about 1 mm. On the other hand, most real-life objects have curved surfaces, and flexible tactile devices are capable of generating microscopic topographical features with different curvatures, which can be used to simulate non-planar morphological features of virtual or remote 3D objects [11].

Depending on different actuation principles, tactile displays that produce microscopic morphology changes can be categorized into electroactive polymers [12], [13], [14], electromagnetic drives [15], [16], shape memory alloys [17], [18], pneumatic [19], [20], [21], [22], [23], [24], [25], [26], [27], and others [28]. Among them, electroactive polymers usually require several kilovolts to generate sufficient deformation, which raises safety-related discussions. Electromagnetic actuators have challenges in miniaturization and flexibilization. Shape memory polymers generally require long response times. Pneumatic actuation methods have the advantages of wide power sources, high output force, and low cost, which have attracted extensive attention from a wide range of scholars.

Pneumatic is tactile display typically a dense array of pneumatic actuators, each comprising an air chamber, a pipe, and a controllable deformation element. By adjusting the pressure inside the air chambers, the deformation elements such as films or pins can be driven to protrude or recede, creating tactile patterns or textures with varying surface morphology. According to the relative positions of the air chambers and pipes, the existing tactile displays based on microscopic morphological changes can be categorized into chamber-pipe homogeneous distribution [19], [20], [21], [22] and chamber-pipe layered distribution [23], [24], [25], [26].

The chamber-pipe homogeneous distribution structure in which the interleaved distribution of air chambers and pipes within the single layer can improve the compactness of the system. King et al. proposed a pneumatic tactile display for surgical robots with a resolution of 5 mm and analyzed the effect of different chamber and film parameters [19]. Robinson et al. developed a sensor-driven integrated pneumatic tactile

Manuscript received 21 August 2023; revised 17 December 2023; accepted 30 January 2024. Date of publication 23 February 2024; date of current version 19 December 2024. This work was supported in part by the National Key Research and Development Program under Grant 2017YFB1002803 and in part by the National Natural Science Foundation of China under Grant 61973016. This paper was recommended for publication by Associate Editor M. Eid and Editor-in-Chief D. Prattichizzo upon evaluation of the reviewers' comments. *(Corresponding author: Dangxiao Wang.)*

This work involved human subjects or animals in its research. Approval of all ethical and experimental procedures and protocols was granted by Biological and Medical Ethics Committee of Beihang University under Application No. BM20220204, and performed in line with the User Experiments on Soft Texture Display.

Boxue Shan, Congying Liu, Yuan Guo, Yiheng Wang, Weidong Guo, and Yuru Zhang are with the State Key Lab of Virtual Reality Technology and Systems, Beihang University, Beijing 100191, China.

Dangxiao Wang is with the State Key Lab of Virtual Reality Technology and Systems, and Beijing Advanced Innovation Center for Biomedical Engineering, Beihang University, Beijing 100191, China, and also with the Peng Cheng Laboratory, Shenzhen 518055, China (e-mail: hapticwang@buaa.edu.cn).

Digital Object Identifier 10.1109/TOH.2024.3367708

device with a spatial resolution of 20 mm [20]. Russomanno et al. proposed a flexible micro-pneumatic tactile display that can simulate touchscreen buttons, with adjacent actuators with center-to-center horizontal and vertical spacing of 13 mm and 14 mm [21]. Heisser et al. proposed a micro-pneumatic tactile display based on a chemical ignition method, with the device consisting of 3∗3 pneumatic actuators with a spatial resolution of 4 mm and a thickness of 3.5mm [22]. However, interference between air chambers and pipes within the single layer limits the maximum alignment density of the air chamber arrays, resulting in a lower spatial resolution (4-20mm) for the tactile device mentioned above. The chamber-pipe layered distribution structure avoids the space congestion caused by the piping and air chamber being on a single layer, and the pneumatic tactile display adopting this structure has an advantage in terms of spatial resolution. Wu et al. and Russomanno et al. designed pneumatic refreshable Braille displays based on this structure with a spatial resolution of 2.5 mm [23], [24], [25]. Haptx develops microfluidic actuator arrays with up to 2.5mm spatial resolution, generating raised deformations in the film that can change surface morphology and provide haptic feedback for gloves [26]. In addition, there is a pneumatic tactile display that realizes a pipeless structure by combining shape memory polymers with a spatial resolution of 4 mm [27], but the actuation requires a long response time of 2.5 seconds.

Most existing pneumatic tactile displays have a spatial resolution equal to or larger than 2.5 mm. For a high-fidelity tactile experience, the ideal spatial resolution should be around 1 mm. [9], [10]. The main reason for this gap is the difficulty in wiring caused by the high-density arrangement of actuators, and the existing pipe distribution strategies are insufficient to support a higher density of chambers. Although the chamber-pipe layered distribution structure avoids spatial interference between air chambers and pipes, mutual interference between pipes is still not negligible. A direct approach is to reduce the cross-sectional dimensions of the pipes to allow for a denser arrangement of pipes in the single layer. However, this reduction in the size of the pipes not only increases the response time but also increases the manufacturing difficulty and cost of the tactile displays. Multi-layer soft lithography and microfluidic 3D printing technologies enable the meticulous creation of complex multi-layered structures [29], [30], facilitating the fabrication of multifunctional microfluidic components and devices. However, this research direction has not yet expanded to include pneumatic tactile displays. The wiring of channels remains a challenge amidst the high-density integration of microfluidic actuators.

In this paper, inspired by multi-layer interchanges, we propose a multi-layer stacked pipe structure with a hierarchical arrangement of pipes, in which the pipes are arranged from bottom to top in accordance with the distal proximity of the air chambers relative to the air inlets. Compared to the structure where the pipes are arranged in a single layer, our proposed structure meets the wiring requirements of high-resolution pneumatic tactile displays and allows the arrangement of air chambers at a higher density. Further, we developed a soft tactile display for high-resolution tactile patterns or textures display based on the proposed structure (spatial resolution of 1.25 mm). By adjusting the input pressure, the bump height of the actuator unit can be controlled independently and continuously. We simulated and experimentally validated the actuator to ensure that the actuator produces sufficient tactile rendering effects under safe air pressure. Quantitative experimental results show that the actuator can generate 0.145 mm out-of-plane displacement and 17.7 mN support force under 1000 mbar pressure. Finally, a user study validated the effectiveness of our high spatial resolution tactile display.

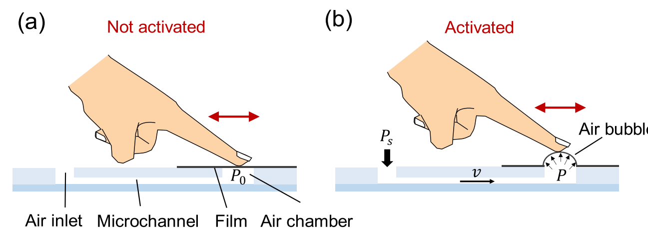

Fig. 1. Working principle of our pneumatic actuator to produce film deformation. (a) The actuator is not driven and the film is flat. (b) The actuator is driven and the film bumps produce deformation.

II. Working Principle and Fabrication Processes

A. Working Principle of Actuator

As shown in Fig. 1(a), the actuator consists of a thin film layer, a structural layer, and a substrate layer, forming a cylindrical air chamber, a microfluidic channel, and an inlet. The chamber and the inlet are interconnected by microfluidic channels to form a complete microfluidic circuit, which is then connected to the pneumatic control system via an external hose (See Section II-E). In the initial state, as the air chamber is at atmospheric pressure, the film is completely flat and the actuator is in an undriven state. Opening the solenoid valve directs the pressure source into the chamber to drive the film to produce a flat profile change. When the chamber pressure is released, the film returns to its initial flat state. The time required for the entire driving process increases as the diameter of the microchannel decreases.

B. Actuator Array Structure Design

In order to integrate individual micro-pneumatic actuators (Fig. 1) into a high-density actuator array, multiple chambers need to be arranged more closely together, with each chamber connected to a separate microfluidic line, giving the actuators independent actuation capability. Taking the 5∗5 actuator array as an example (Fig. 2(a)), the pipes connecting the inner chambers lead from between the outer chambers, and the center distance of the adjacent chambers can be expressed as:

$$R_A = 2\left(r + m_{cp}\right) + l \tag{1}$$

where R refers to the centre distance of the air chamber, r refers to the radius of the chamber, m refers to the wall thickness between the chamber or pipe, which is determined by the modulus of the material and the input pressure and l refers to the width of

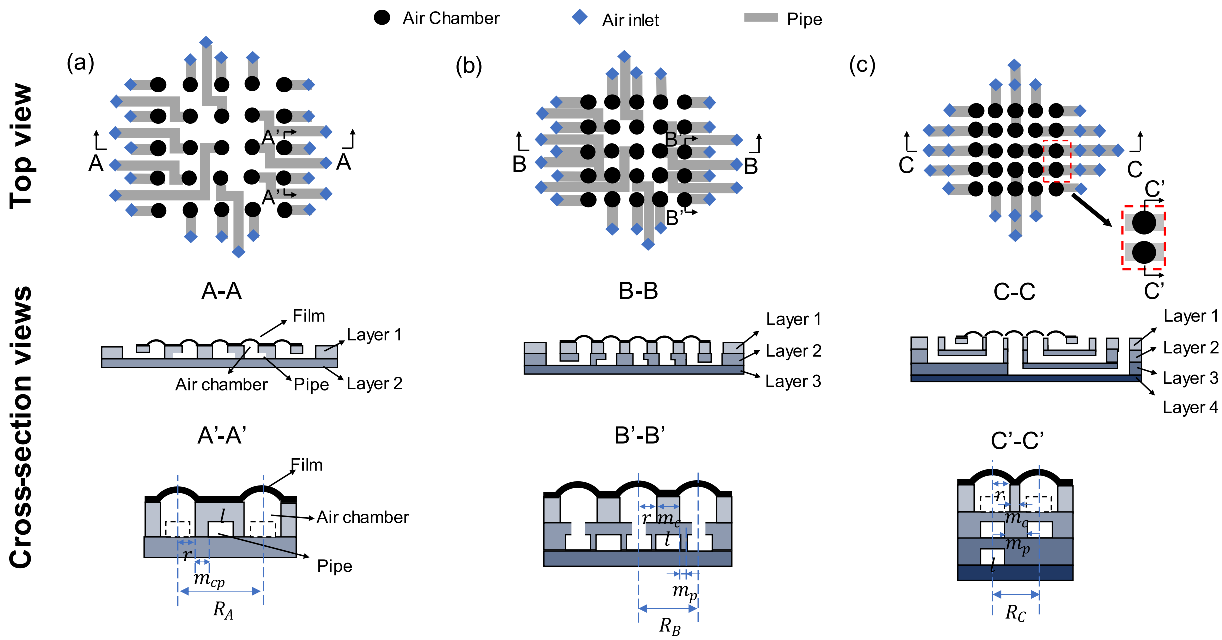

Fig. 2. Different chamber-pipe distribution structures. (a) Chambers and pipes on the single layer (lower density). (b) Chambers and pipes on different layers (medium density) and (c) A multilayer stacked pipe structure with a hierarchical arrangement of pipes (higher density).

the pipeline which is determined by a combination of preparation process capabilities and drive response speed requirements.

Since the pipes are led through between the chambers, the presence of the pipes limits the minimum center distance between adjacent chambers and does not further increase the integrated density of the array. In order to reduce the influence of the pipes on the density of the air chamber arrangement, the researchers distributed the air chambers and pipes in different layers, and the following is a discussion of the 5∗5 actuator array structure with a layered distribution of chambers-pipes, as shown in Fig. 2(b). In this case, the center distance of the air chambers can be expressed as:

$$R_B = \text{Max}\left[2\left(m_p + l\right), 2r + m_c\right] \tag{2}$$

The theoretical minimum center distance of adjacent chambers R_B depends on the relationship between the size of the chamber layer structure and the pipe layer structure. For larger chamber radius r and chamber wall thickness m_c, the influence of the pipes dimensions on the density of the chamber arrangement can be ignored, but with the improvement of the spatial resolution requirements, r and m_c gradually decrease, at this time, the maximum density of the arrangement of the chambers is mainly affected by the lower layer of the pipeline dimensions of the width l and the wall thickness m_p between the pipes.

As shown in Fig. 2(c), In order to further reduce the influence of the pipe width l and wall thickness m_p between the pipes to improve the spatial resolution of the device, we adopt a structural layout with a layered arrangement of pipes to further reduce the influence of pipe sizes l and wall thicknesses m_p between pipes, at which time, the center distance of the chamber can be expressed as:

$$R_C = Max\left[m_p + l, 2r + m_c\right] \tag{3}$$

It can be seen that the theoretical minimum center distance of the air chamber is $m_p + l$. Compared with the pipe structure in Fig. 2(b), under the condition of the same pipe size l and piping wall thickness m_p, the pneumatic tactile device with the pipe layered distribution structure can theoretically double the spatial resolution or achieve a faster response speed under the same resolution.

The air chamber and microfluidic channel of the innermost actuator are encapsulated by the substrate layer to form a closed microfluidic circuit. As the actuator array expands, the channels connected to the external actuators are arranged upward accordingly until a sufficient number of actuators are produced, from which it can be obtained that the relationship between the maximum number of actuators and the number of structural layers satisfies the following equation, taking a square array and hexagonal array as examples.

$$N = (2n - 1)^2 \ (n \geq 1) \tag{4}$$

where N refers to the maximum number of actuators for the square array, and n refers to the number of structural layers.

In the above, we have listed only the design methods for a square actuator array. By using a multi-layer stacked fluid circuit design method, designers can develop a wide variety of array layout patterns to suit different needs. The microfluidic circuits between different layers are spatially driven in parallel, and from the equation (4), it can be seen that the number of corresponding actuators grows exponentially with the stacking of loop layers, which can meet the demand of texture display interface for the huge number of actuators.

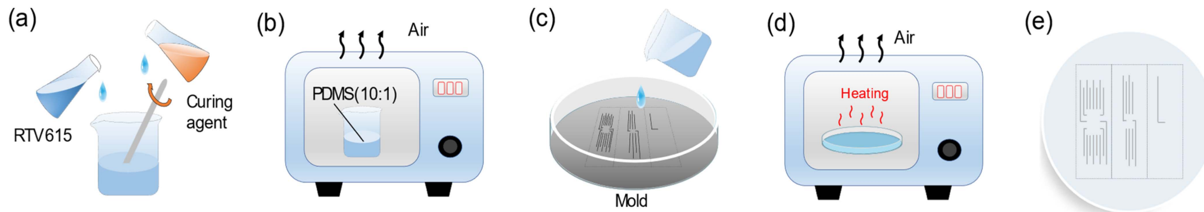

Fig. 3. Microfluidic chip fabrication process. (a) Mixing and stirring of PDMS solution. (b) Removing air bubbles from mixed PDMS solution. (c) Casting Mold. (d) Vacuuming and then heating to cure. (e) A PDMS chip with three microchannel structures.

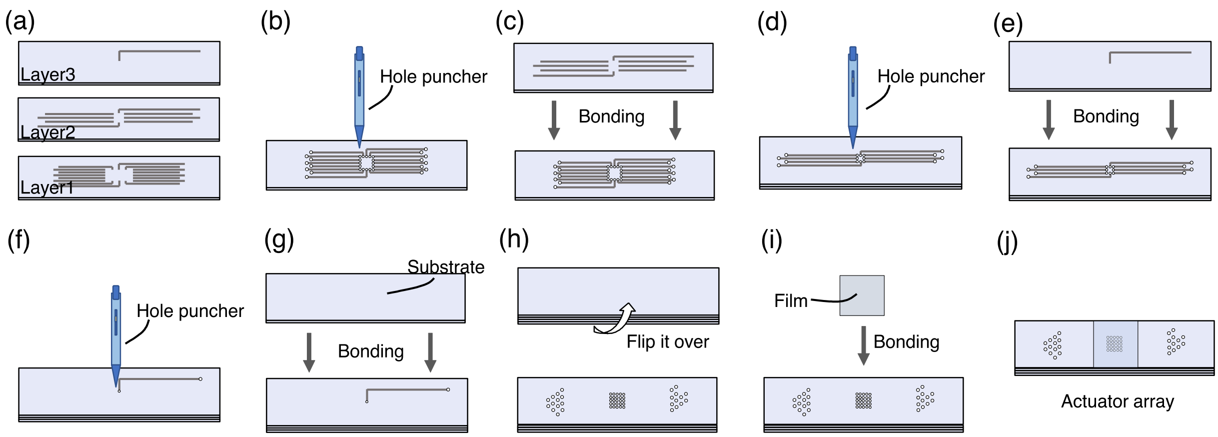

Fig. 4. Hole punching and bonding process. (a) Cutting the whole chip into individual pieces. (b) Perforating the layer1. (c) Bonding the layer2 to the layer1 (perforated). (d) Perforating the layer1&2. (e) Bonding the layer3 to the layer1&2 (perforated). (f) Perforating the layer1&2&3. (g) Bonding the substrate layer to the layer1&2&3 (perforated). (h) Flipping it over. (i) Bonding the film to the layer1&2&3 and substrate layer. (j) Microfluidic actuator array.

C. Fabrication of Actuator Array

1) Soft Lithography Fabrication Process (Fig. 3): First, the PDMS solution (RTV615) and curing agent were mixed in a 10:1 mass ratio and stirred for 10 minutes using a mixer to obtain a uniformly mixed PDMS solution (Fig. 3(a)). Then, the uniformly mixed PDMS solution was placed in the vacuum oven for evacuating vacuum for 15 minutes until there are no air bubbles in the solution (Fig. 3(b)), pour the mixed PDMS solution after excluding the air bubbles slowly into the mold (Fig. 3(c)), which is prepared by a soft lithography process containing three different structures, after that, place the mold in the vacuum oven for second vacuuming for 10 minutes to exclude the air bubbles generated during the casting process, place the mold after casting on vacuum oven and cure it at 65°C for 10 minutes (Fig. 3(d)). Finally, the cured PDMS is peeled off from the mold to obtain a chip containing three microchannel structures. (Fig. 3(e)).

2) Hole Punching and Bonding Stacking Process (Fig. 4): Firstly, cut the whole chip into individual pieces (Fig. 4(a)), and structural layer 1 was perforated to form cylindrical cavities through the end of the microfluidic channels of layer 1, which were used to form the air chambers and air inlets (Fig. 4(b)).

Then, the perforated structural layer 1 and structural layer 2 were ultrasonically cleaned in anhydrous ethanol reagent for 10 minutes, removed and placed in an oven for drying, and bombarded in an oxygen plasma cleaner for 15 seconds. The perforated structural layer 1 and the unperforated structural layer 2 were aligned and laminated together by gently pressing the laminated surface with tweezers, and placing it in a vacuum drying oven at 65°C for 30 minutes after bonding, and structure layer 1 and structure layer 2 form an irreversible seal to complete the microfluidic cavities encapsulation process of the outermost 16 microfluidic actuators (Fig. 4(c)), and then punch the hole of the bonded structural layer 12, corresponding to the end of the microfluidic channels of the structural layer 2 through the cylindrical cavities (Fig. 4(d)), and layer 3 is bonded to complete the microchannel encapsulation process of the middle 8 microfluidic actuators (Fig. 4(e)), the bonded structural layer 123 is perforated and the end of the microfluidic channel of the corresponding layer 3 forms a cylindrical cavity (Fig. 4(f)). The whole structural layer is bonded to the bottom plate to complete the microchannel encapsulation process of the innermost microfluidic actuator (Fig. 4(g))

Finally, using a glass spin-coated 10:1 PDMS film, the film was bonded to the surface of 25 air chambers exposed after flipping (Fig. 4(h)) to complete the irreversible sealing of the film, structural layer, and substrate layer (Fig. 4(i)), and finally obtain a 5×5 microfluidic actuator array that can be actuated individually (Fig. 4(j)).

D. Fabrication Parameters of Actuator Array

As shown in Fig. 5(a) and Table I, the overall size of the device is 70 mm $\times$ 20 mm $\times$ 4 mm. The device integrates a 5×5 actuator array, and the spatial resolution is defined

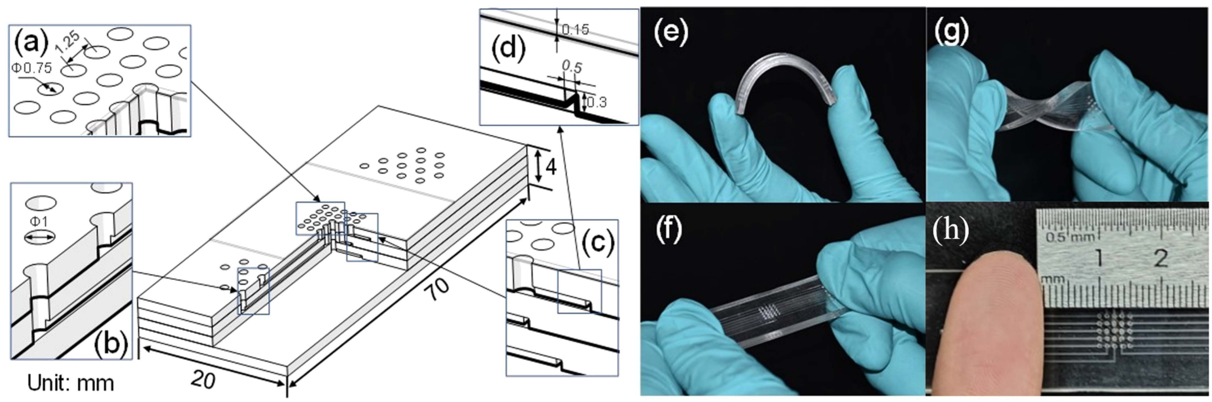

Fig. 5. Overall structure of the proposed actuator array. (a) The diameter of the air chamber is 0.75 mm and the spatial resolution is 1.25 mm. (b) Air inlet diameter and detailed structure. (c) Detail view of the microchannels. (d) The size of the microchannel and the thickness of the film. (e) Bending, (f) Stretching and (g) Twisting characteristics of the device. (h) The detail view of the 5 × 5 actuator array compared with a human index fingertip and the center distance between adjacent air chambers is 1.25 mm.

TABLE I
MAIN FABRICATION PARAMETERS

Type	Result
Total size	70 mm×20 mm×4 mm
Spatial resolution	1.25 mm
Air chamber diameter	0.75 mm
Thickness of film	150 μm
Size of the microchannels	500 μm×300 μm
Maximum drive pressure	1000 mbar
Material	RTV615

as the center distance between adjacent actuator chambers. As shown in Fig. 5(a), the center distance between adjacent air chambers is 1.25 mm, each chamber is 0.75 mm in diameter and the height varies with the number of layers in the range of 1 mm to 3 mm. The device is made of polydimethylsiloxane (PDMS) through multilayer bonding, the soft polymer material has good insulation properties, durability, and mechanical properties close to human skin, and has been widely used in human-computer interaction devices [31], [32]. The RTV615 solution and curing agent are mixed in a 10:1 (most common) mass ratio.

To facilitate the fabrication, the microfluidic channel is designed with a rectangular cross-section, in which, in order to reduce the longitudinal deformation of the cavity channel during the driving process, we reduce the height of the cross-section and increase the distance between the microchannel and the upper surface. The final size of the channel cross-section was 500 μm × 300 μm. Subsequent subjective experiments with participants claimed not to perceive longitudinal deformation caused by the channel.

In addition, PDMS films prepared using the spin-coating process have a smooth and flat surface that provides a natural feel and comfort when in contact with the skin, making them ideal for use on the surface portion of devices that come into contact with people. Therefore, we used PDMS material to design the topmost surface film. The thickness of the film affects the height of the film projection. The thickness of the film affects the height of the film projection. We used commercial software COMSOL Multiphysics 6.0 to study the mechanical characteristics of the flexible PDMS (10:1) film in the actuator. The strain distributions were discussed for the actuator under different input pressures. Considering the impedance effect of the surrounding material when the film bulges, a 3D model was constructed as follows: a rectangular body with dimensions of 4500 × 4000 × 700 μm was created, and a cylindrical cavity with a radius of 375 μm was removed from the bottom, forming a cylindrical film with a radius of 375 μm and a thickness of 150 μm on the rectangular body. A point in the center of the surface was fixed to measure the height of the film bulge using derived values. We applied a fixed constraint to the bottom surface of the rectangular body, and a normal pressure P (Pa) was applied to the lower surface of the film. At the initial state, both the displacement field and the structural velocity field were set to zero. The solid mechanics field was employed to investigate a steady-state problem, in which structural mechanics and nonlinear structural materials modules were utilized. A highly refined free tetrahedral mesh was adopted with adaptive mesh refinement, with a maximum refinement level of 5 and an element growth factor of 1.7. In the finite element analysis, the Mooney-Rivlin energy potential model was used to specify the PDMS model as a hyperelastic material. The elastic modulus (E) and poisson's ratio (v) used in the analysis were E = 750 kPa, v = 0.45 for PDMS (10:1) [33]. In order to obtain multiple solutions simultaneously, we performed a parametric scan for the input pressure P. The relative tolerance of the steady-state solver was set to 0.001, and the fully-coupled linear solver PARDISO had a maximum iteration limit of 25. z-axis coordinates of the central point of the film were obtained at different input pressures. Simulation results showed that for a 150 μm thick PDMS (10:1) film (Fig. 7(b)), under an input pressure of 1000 mbar, a perceptible out-of-plane displacement of 158 μm can be generated.

E. Control Method of Actuator Array

We used an air pressure control system to independently drive the 5 × 5 actuator array. The system consists of an air pump, a safety valve, a check valve, a pressure sensor (pressure

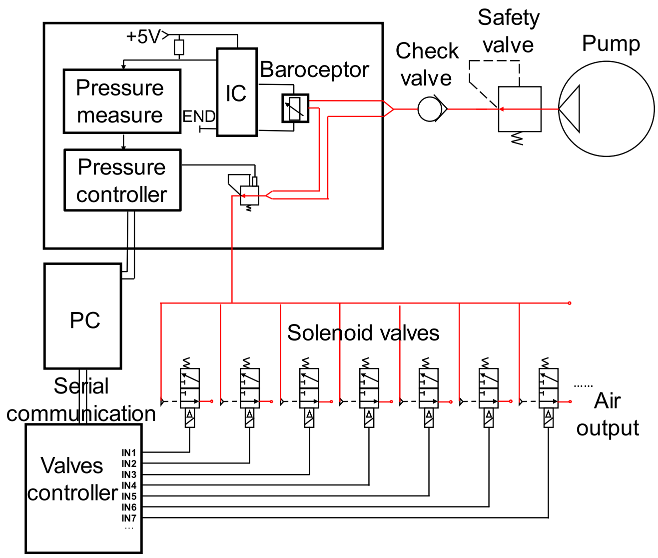

Fig. 6. Air pressure control system of the actuator array, the red line is the air connection line.

measurement module), a pressure controller, twenty-five solenoid valves (two-position three-way), a solenoid valve controller, and a computer (Fig. 6). The air is shunted by a 1-to-25-way solenoid valve module and flows to the 25 actuator units to achieve independent actuation of the 25 actuators.

In the control system, the host PC is connected to the pressure controller module and the solenoid valve controller module respectively through the serial port, which can set the output pressure value of the system. It can also control the opening and closing of the solenoid valve manually. The air pump provides the initial air pressure of 3000 mbar to the system, and after the pressure-reducing valve and check valve, it enters the air pressure control module. The module is equipped with a barometric pressure sensor module ($< 6\%$ FS), which can monitor the air pressure in the pipeline in real-time and be used for output pressure correction. The airflow from the air pressure control module maintains the set value ($< 0.02\%$ FS). It passes through the solenoid valve module and hose into the chamber channel of the actuator unit to achieve constant pressure drive to the actuator.

In order to ensure the safety of use and prevent overpressure from film bursting or film bond failure, the safe air pressure for use was determined through the failure threshold experiment, which will provide a clear range of operating pressures for the actuator array. For the failure pressure threshold experiment, a random selection of 10 actuators was made from the 5×5 actuator array. The initial pressure was set to 1000 mbar, with a pressure increment of 25 mbar. Following each pressure increment, a 30-second interval was observed to monitor the state of the actuators. This procedure was repeated until the thin film ruptured or the bond failed. Subsequently, the failure pressures of the 10 randomly selected actuators were documented. The average failure pressure threshold of 1265 mbar and a standard deviation of 88.9 mbar.

Film deformation affects tactile performance to a certain extent. To ensure consistent performance of each actuator that produces a tactile pattern, we connect all the solenoid valves in parallel to the same pressure channel to ensure that the pressure inside the chamber to which each open channel is connected is the same, which in turn ensures the consistency of the normal displacement of the film.

III. Characterization of Actuator Array

A. Displacement

As mentioned in Section II-A, the principle of this actuator is that air pressure drives the film to produce deformation, and this section explores the change of film bump displacement with the input air pressure. Due to the high transmittance of PDMS material, it is difficult to measure the film without surface transmittance treatment by optical means. In order to make accurate measurements without changing the material properties of the film, we use a contact measurement test bench (Fig. 7(a)) to sample the bump height at different air pressures. The test bench includes a force transducer (100 g, AR-WM10s, China), a high precision 3-axis adjustment platform ($\pm$ 6.5 mm, HLD40, China) and a standing platform.

The operation method is as follows: first, the force sensor is zeroed, and the force sensor is continuously brought closer to the film surface through the three-axis adjustment platform until the force sensor indication changes, and the micrometer indication is recorded as the initial height of 0 mm. After that, open the solenoid valve, inflate the air chamber, gradually increase the distance in the Z-axis direction until the sensor indication reappears as 0 N. Finally, the difference between the final micrometer indication and the initial indication is recorded as the bump height of the film. We used this method to measure the bump height for five random actuators, the results are shown in (Fig. 7(b)). As the input air pressure increased from 0 to 1000 mbar, the average bump height increased from 0 μm to 145 μm. The experimental results are similar to our results through COMSOL simulation, and there is almost a linear relationship between the film displacement and the air pressure value, which is the same as the previous experimental conclusions [22]. In addition, the small error in film displacement above the different air chambers ensures the consistency of the user's tactile experience during finger interaction with the device.

B. Force

We further tested the support force of the actuator to measure the relationship between the support force and the magnitude of the input pressure. In the experiment, we put the force sensor in contact with a flat film surface and gave a pre-pressure of 2 mN, zeroed the force sensor indication at this time, and recorded this moment as the initial state, after which the air pressure was continuously increased from 0 mbar to 1000 mbar through the pressure controller, and recorded the force at the same time, we randomly selected five actuators for measurement and obtained the average output force of the actuators. As shown in Fig. 7(c),

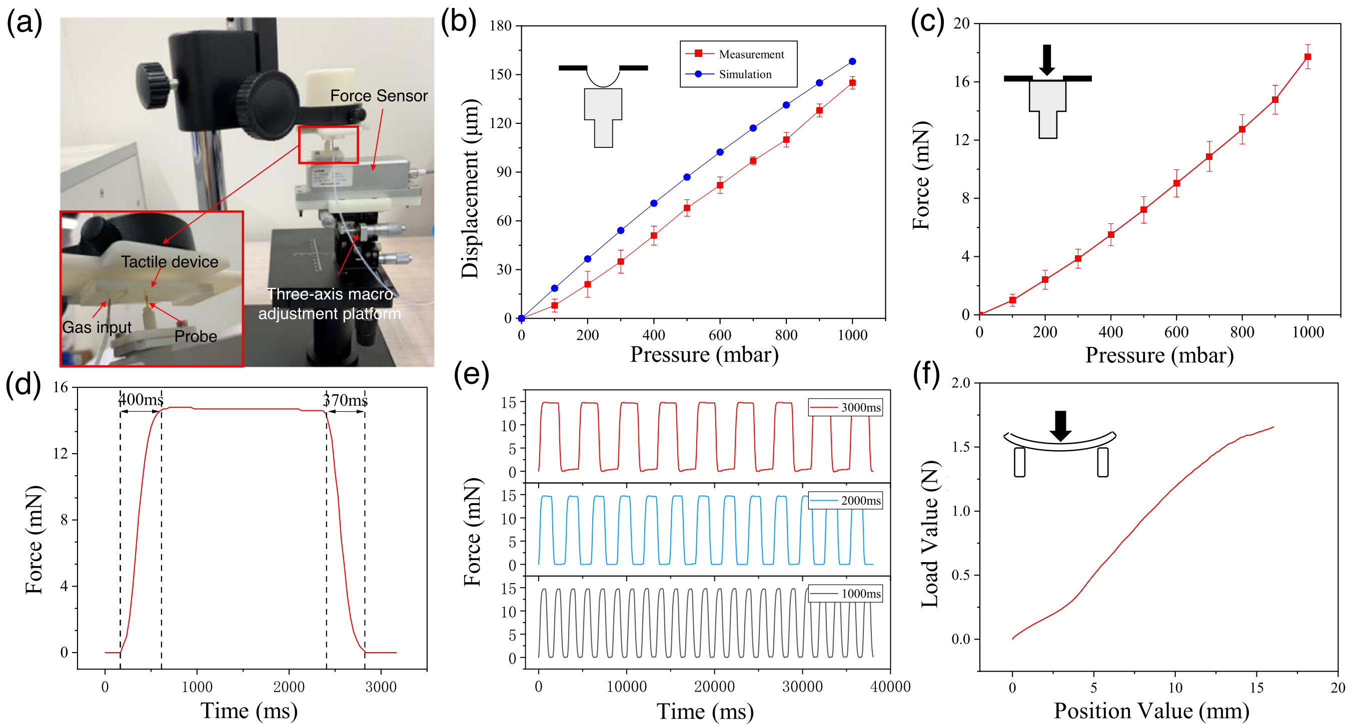

Fig. 7. Quantitative experiments with tactile devices. (a) Measurement devices and operation details of the Experimental bench. (b) Effect of input air pressure on the height of film bulge. (c) Effect of input air pressure on output force (i.e., when displacement is zero). (d) Response time of the pneumatic actuator in one work cycle. (e) Dynamic response of the actuator in 1000 ms, 2000 ms, and 3000 ms operating cycles. (f) Stiffness test of the device.

we can see that the output force increases almost linearly with increasing pressure, and the maximum force of 17.7 mN is obtained at 1000 mbar.

C. Dynamic Response

By using the experimental bench (Fig. 7(a)), we further evaluated the dynamic performance of the actuator using the same tactile device, including response time and repeatability at different duty cycles. In one duty cycle, after the applied air pressure increased from 0 mbar to 900 mbar, at which time the solenoid valve was opened, the pressure in the air chamber increased rapidly to the target pressure within 400 ms and generated a force of 14.7 mN (Fig. 7(d)). After two seconds, the solenoid valve was closed and the pressure in the air chamber returned to the initial value from the target pressure within 370 ms. By varying the activation cycle of the solenoid valve and repeating the above working cycle several times, we can obtain the repeatability and stability of the device at different working cycles (Fig. 7(e)), and it can be observed that the pneumatic actuator is always able to activate and close synchronously and repeatedly at different working cycles.

D. Flexibility and Stretchability

To investigate the softness of the haptic device under this PDMS material fabrication parameter, the device was tested for three-point bending stiffness using a tensile testing machine (100 N, ZGDR, China). The actuator was loaded using a uniform speed of 5 mm/s with a distance of 53 mm between the support points. The relationship between the measured output force and displacement was obtained (Fig. 7(f)).

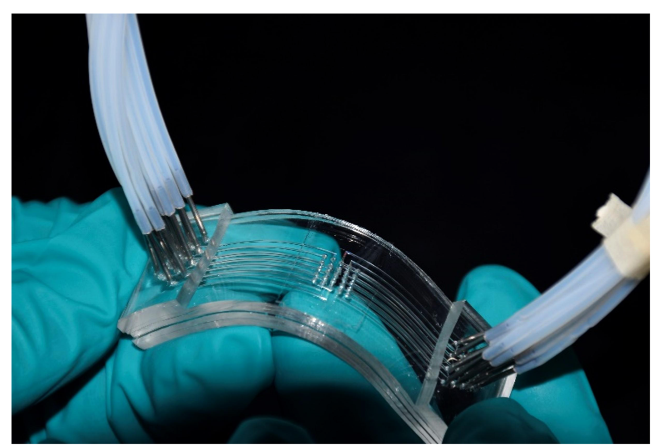

Fig. 8. Actual pictures of working on curved surfaces. When the tactile device is in a bent state, the microfluidic unit can still be raised a certain displacement and form a stable pattern or low frequency vibration (up to 10 Hz).

The material of the texture rendering device is RTV15 with a 10:1 primary agent ratio and a thickness of about 4 mm. Benefiting from the soft material properties, the tactile device in this paper is competitive in terms of flexibility and stretchability, and the soft characteristics of the device are depicted in Figs. 5(e), (f), (g) and 8. It can be seen that the actuator array can produce deformation such as bending, tensile and twisting without damage. In addition, when the actuator array is in a bent or twisted state, it can still produce a stable textured surface.

TABLE II
COMPARISON BETWEEN OUR DEVICE AND OTHER PNEUMATIC TACTILE DEVICES IN TERMS OF FIVE MAIN FEATURES

Tactile Device	Structure Type	Spatial Resolution (mm)	Array size	Soft/Rigid	Effective Surface Area(mm^2)	Vertical Displacement (mm)
[19]	Chambers & pipes on the single layer	5	3*2	Soft	12.57	2.42
[20]		20	2*2	Soft	50.27	~16.3
[21]		13-14	2*3	Soft	44.18	3.0
[22]		4	3*3	Soft	7.07	0.50
[24]	Chambers & pipes on different layers (pipes on the single layer)	2.5	2*3	Rigid	1.77	0.56
[25]		2.5	7*8	Rigid	1.77	0.50
[26]		⩾2.5	135	Soft	Unknown	⩽1.5
[27]	Pipeless structure	4	32*24	Soft	7.07	0.50
Our device	Multi-layer stacked pipe structure	1.25	5*5	Soft	0.44	0.21

Benefiting from this excellent soft characteristic, the device can be affixed to surfaces of different curvatures to suit different application scenarios, thus providing users with tactile feedback in rich scenarios.

IV. USER EVALUATION

A. Absolute Threshold Experiment

We conducted a bump height perception threshold test with the proposed device to see if participants could perceive the tactile stimuli produced by the actuators. 10 participants were recruited from Beihang University to participate in this tactile test (8 males and 2 females, aged between 23 and 27 years), all of them with the right hand as their dominant hand, and they were introduced to the purpose and procedure of the experiment and signed a written consent form. All participants were free of any perceptual deficits. The experiment was approved by the State Key Laboratory of Virtual Reality Technology and Systems of China and was in accordance with ethical standards.

The device was fixed to the table, participants placed their index fingers on the texture presentation area. During the experiment, participants were allowed to perform sliding exploration, and the study measured the absolute threshold of texture, i.e., the minimum height of the bump at which the finger could reliably feel the actuator feedback.

User physiological-psychological experiments were conducted using transformed up-down methods [34], which are known to produce thresholds at 79.4% of the psychometric function in a one-up and three-down scheme. The specific steps are: first give an initial height and ask participants if they can feel the film bump, if they successfully detect the tactile signal three times in a row, reduce the input air pressure, if participants do not feel the tactile signal, increase the input air pressure, and as the number of trials increases, the pressure step gradually decreases until it converges to the 79.4% success rate threshold. We set the initial pressures to $P_{01} = 600$ mbar and $P_{02} = 100$ mbar. The subsequent step sizes are defined as follows:

$$T_i = \begin{cases} \frac{P_{01-}P_{02}}{i} \ (i \leq 8) \\ 63 - 5\,(i-8) \ \ (i > 8) \end{cases} \tag{5}$$

where T_i refers to the step size of the *i* th reversal and *i* refers to the number of reversals.

Larger steps were used for the first few inversions to quickly bring the stimulus level closer to the estimated threshold. After more than 8 reversals, smaller steps were used for the remaining inversions to improve the accuracy of the estimated threshold, continuing until the pressure values converged ($\mathrm{T_i} \leq 10$ mbar) or until 50 trials were reached. If convergence had not occurred after 50 trials, the number of trials would be increased accordingly until convergence was achieved. Eventually, we found the pressure value at each reversal, and to exclude the effect of instability of the first few reversals, we averaged the pressure values of the last 8 reversals to obtain the 79% average threshold pressure value (Fig. 9(b)).

Each participant was asked to participate in two sets of 25 trials each, and at the end of each set, participants were asked to rest for two minutes, taking approximately 45 minutes per participant for the entire experiment. Throughout the experiment, participants were blindfolded to prevent interference from visual cues. The results of the first experiment are shown in Fig. 9(b). The threshold air pressure was 191 mbar $\pm$ 57 mbar, corresponding to a bump height of 19.8 μm $\pm$ 7.4 μm. Among all users who participated in the experiment, the maximum air pressure threshold was 229 mbar and the minimum threshold was 112.5 mbar.

B. Texture Patterns Discrimination

To validate the ability of the device to present tactile patterns, we set up 8 typical patterns for user pattern recognition experiments (Fig. 9(e)), and we used a 5×5 actuator array (1.25 mm spatial resolution) and 1000 mbar air pressure (above the tactile stimulation threshold) to dynamically generate these patterns. A total of 10 participants, and 8 males and 2 females, with a mean age of 24 years, all of whom were right-handed and none of whom reported any history of neurological disease or physical impairment that could affect hand function, were recruited for this trial, and all participants signed a written consent form to participate in the study.

During the experiment, participants were seated at a table and allowed to use their right index finger to explore the surface of the device by touch, and each person was required to go through a 5-minute training session for 8 patterns before the experiment formally began. We generated all patterns randomly for the

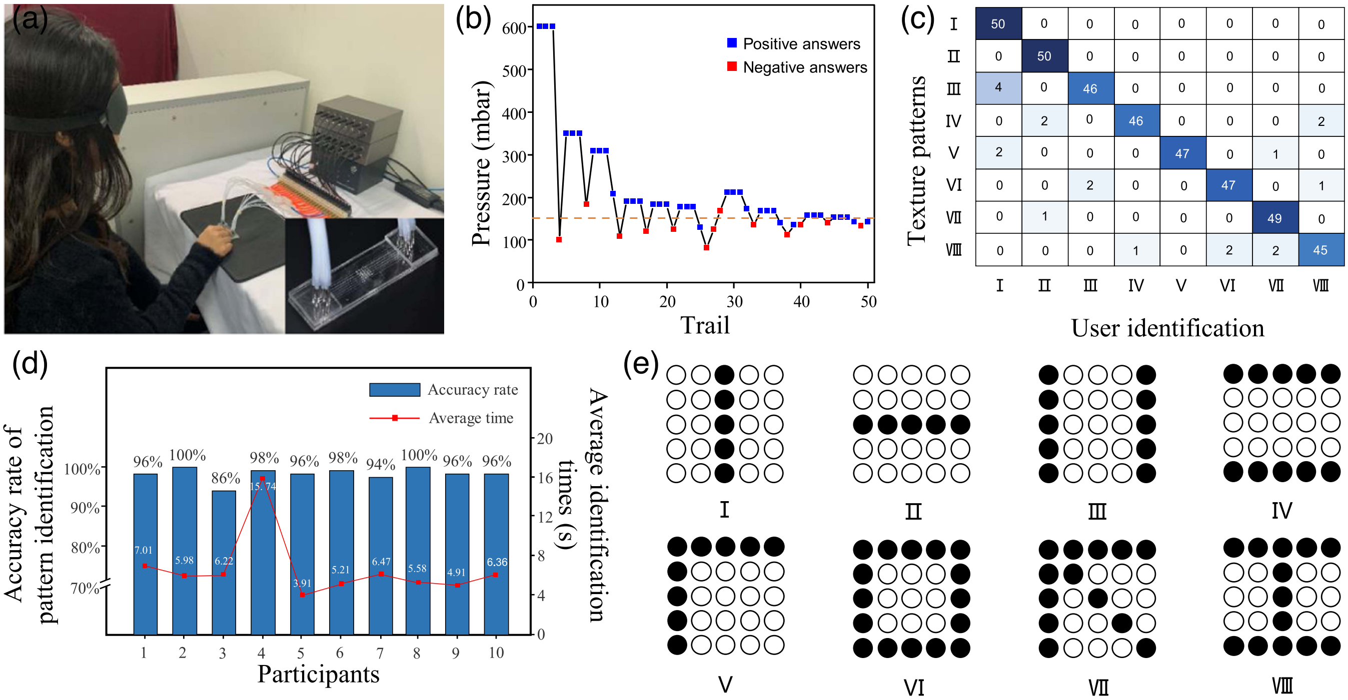

Fig. 9. User evaluation of the actuator array. (a) The scene of the subjective experiment. (b) Enter pressure threshold trials. (c) Confusion matrix for all participants. (d) Average accuracy and time for participants to identify the eight texture patterns. (e) Eight texture patterns for texture identification.

participants, who were blindfolded to prevent the interference of visual cues. The type of pattern touched was verbally informed by the participant and the time taken for the entire recognition process was recorded. Participants were allowed to repeatedly slide their fingers over the textured surface throughout the experiment. The results of the confusion matrix reporting experiment showed (Fig. 9(c)) that the unit values along the diagonal were significantly larger than the other units that distinguished the cases. In addition, we calculated the accuracy of texture recognition and the average time spent by each participant. As shown in Fig. 9(d), among all participants, the texture recognition accuracy ranged from a maximum of 100% to a minimum of 86%, with an average accuracy of 96%. The average recognition time of the participants was 6.74 seconds, the minimum average recognition time was 3.91 seconds, and the maximum recognition time was 15.74 seconds. Based on the feedback from participants after participating in the experiment, we also knew that the tactile patterns felt throughout the recognition process were smooth and continuous, illustrating that the texture display device with 1.25 mm spatial resolution can render fine texture patterns.

V. Discussion

During the testing process of objective experiments (Fig. 7), we found that the failure form of the actuator was mainly manifested as two cases of film rupture and bonding failure, and our subsequent set of experiments measured a film failure pressure of 1200 mbar, corresponding to the maximum bump height of 0.21 mm and the maximum support force of 26.3 mN. Considering the safety of interaction and the stability of the device, we generally take a driving air pressure lower than 1000 mbar for driving.

Due to the high spatial resolution of the device, the distance between the centers of adjacent chambers is narrowed and thus the diameter of the chambers and the surface film is limited (0.44 mm^2), which leads to constraints on the bump height and force. We demonstrate the ease of perception of the device in presenting texture effects through user experiments (Fig. 9), where a bump height of 0.1 mm or more can produce a robust haptic experience, and the support force, although only 17.7 mN, produces better-than-indicator effects. We speculate that the actuator in this paper has a smaller contact area with the finger compared to other devices, and thus produces greater local pressure, which may further enhance the haptic intensity.

In addition, we compared our device with existing haptic devices with dynamic texture generation capability (as shown in Table II). 1.25 mm resolution can produce a more delicate texture surface and generate a richer haptic experience, and compared with rigid haptic devices, the proposed soft haptic device is safe, thin, and adaptable, with the ability to work stably on different surfaces and in different environments. This design change makes our prototype more compact and the high resolution makes more actuators integrated per unit area. Accordingly, more control valves are needed for independent control of the actuators. The application areas of our work might be somewhat limited by the use of research-grade bulky valves and pumps. By embedding the valves and pumps in a control cabinet, our high-resolution tactile devices can be used as desktop interactive devices, for example, high-resolution tactile graphical displays designed for the visually impaired or tactile indicators for cockpit interactions. At present, our primary focus is on the design and implementation of high-resolution tactile device. We believe that by incorporating micro pumps and valves, our high-resolution tactile devices can become more portable, thereby expanding the range of application scenarios.

VI. Conclusion

In this paper, a three-dimensional multi-layer distribution structure for pneumatic channels wiring is proposed to achieve high-resolution pneumatic tactile displays. Our structure consists of a vertically bottom-top order for the actuated units from the center to the boundary of the array, i.e., the pipes of the external units in the array are arranged on top of the pipes of the internal units in the array. This structure can ensure no interference between the pipes of micro pneumatic actuators. The specific air chamber positions corresponding to each layer of piping alignment as well as the sequential order of stacking and punching are integrated within the compact area of a fingertip. We further improve the spatial resolution of the pneumatic tactile displays (1.25 mm). Thanks to the use of soft materials, the device in this paper can produce texture patterns stably under a certain bending state, which can be endowed with different curvature surface texture characteristics. It can also simulate vibrations up to 10 Hz to produce a rich tactile experience. Due to the features mentioned above, the proposed tactile display is expected to be applied to high resolution texture displays, high resolution texture skins, and multimodal tactile displays to enhance the immersion of VR/AR application scenarios.

References

[1] P. Kapur, M. Jensen, L. J. Buxbaum, S. A. Jax, and K. J. Kuchenbecker, "Spatially distributed tactile feedback for kinesthetic motion guidance," in *Proc. IEEE Haptics Symp.*, 2010, pp. 519–526, doi: 10.1109/HAPTIC.2010.5444606.

[2] D. Wang, K. Ohnishi, and W. Xu, "Multimodal haptic display for virtual reality: A survey," *IEEE Trans. Ind. Electron.*, vol. 67, no. 1, pp. 610–623, Jan. 2020, doi: 10.1109/TIE.2019.2920602.

[3] G. C. Bettelani, G. Averta, M. G. Catalano, B. Leporini, and M. Bianchi, "Design and validation of the readable device: A single-cell electromagnetic refreshable braille display," *IEEE Trans. Haptics*, vol. 13, no. 1, pp. 239–245, Jan.-Mar. 2020, doi: 10.1109/TOH.2020.2970929.

[4] J. C. Koone et al., "Data for all: Tactile graphics that light up with picture-perfect resolution," *Sci. Adv.*, vol. 8, no. 33, pp. 2640–2650, Aug. 2022, doi: 10.1126/sciadv.abq2640.

[5] C. Shultz and C. Harrison, "Flat panel haptics: Embedded electroosmotic pumps for scalable," in *Proc. CHI Conf. Hum. Factors Comput. Syst.*, 2023, pp. 1–16, doi: 10.1145/3544548.3581547.

[6] B. K. Johnson et al., "A multifunctional soft robotic shape display with high-speed actuation, sensing, and control," *Nature Commun.*, vol. 14, Jul. 2023, Art. no. 4516, doi: 10.1038/s41467-023-39842-2.

[7] X. Tao, "Virtual and augmented reality enhanced by touch," *Nature*, vol. 575, no. 7783, pp. 453–454, Nov. 2019, doi: 10.1038/d41586-019-03506-3.

[8] S. Mel and M. V. Sanchez-Vives, "Enhancing our lives with immersive virtual reality," *Front. Robot. AI*, vol. 3, Dec. 2016, Art. no. 74, doi: 10.3389/frobt.2016.00074.

[9] F. Vidal-Verdu and M. Hafez, "Graphical tactile displays for visually-impaired people," *IEEE Trans. Neural Syst. Rehabil. Eng.*, vol. 15, no. 1, pp. 119–130, Mar. 2007, doi: 10.1109/TNSRE.2007.891375.

[10] N. Garcia-Hernandez, F. Bertolotto, F. Cannella, N. G. Tsagarakis, and D. G. Caldwell, "How tactor size and density of normal indentation tactile displays affects grating discrimination tasks," *IEEE Trans. Haptics*, vol. 7, no. 3, pp. 356–366, Jul.-Sep. 2014, doi: 10.1109/TOH.2014.2309128.

[11] Y. Guo, Q. Tong, P. Zhao, Y. Zhang, and D. Wang, "Electromagnetic-actuated soft tactile device using a pull–push latch structure," *IEEE Trans. Ind. Electron.*, vol. 70, no. 10, pp. 10344–10352, Oct. 2023, doi: 10.1109/TIE.2022.3217582.

[12] N. T. Ankit, M. Rajput, N. A. Chien, and N. Mathews, "Highly transparent and integrable surface texture change device for localized tactile feedback," *Small*, vol. 14, no. 1, Nov. 2017, Art. no. 1702312, doi: 10.1002/smll.201702312.

[13] H. Phung et al., "Tactile display with rigid coupling based on soft actuator," *Meccanica*, vol. 50, pp. 2825–2837, Nov. 2015, doi: 10.1007/s11012-015-0270-5.

[14] E. Leroy, R. Hinchet, and H. Shea, "Multimode hydraulically amplified electrostatic actuators for wearable haptics," *Adv. Mater.*, vol. 32, no. 36, Jul. 2020, Art. no. 2002564, doi: 10.1002/adma.202002564.

[15] J. Kim, B. K. Han, D. Pyo, S. Ryu, H. Kim, and D. S. Kwon, "Braille display for portable device using flip-latch structured electromagnetic actuator," *IEEE Trans. Haptics*, vol. 13, no. 1, pp. 59–65, Jan. 2020, doi: 10.1109/TOH.2019.2963858.

[16] Y. Guo et al., "MRS-Tex: A magnetically responsive soft tactile device for texture display," *IEEE Trans. Ind. Electron.*, vol. 69, no. 11, pp. 11531–11540, Nov. 2022, doi: 10.1109/TIE.2021.3120490.

[17] A. Singhal et al., "Application of shape memory alloy (SMA) based actuation for refreshable display of braille," in *Proc. ASME Int. Des. Eng. Tech. Conf. Comput. Inf. Eng. Conf.*, 2013, Paper V004T08A053, doi: 10.1115/DETC2013-13159.

[18] P. Sapra et al., "Refreshable braille display using shape memory alloy with latch mechanism," in *Proc. ASME 2017 Int. Des. Eng. Tech. Conf. Comp. Info. Eng. Conf.*, 2017, Paper V009T07A040, doi: 10.1115/DETC2017-68311.

[19] A. Russomanno, Z. Xu, S. O'Modhrain, and B. Gillespie, "A pneu shape display: Physical buttons with programmable touch response," in *Proc. IEEE World Haptics Conf.*, 2017, pp. 641–646, doi: 10.1109/WHC.2017.7989976.

[20] R. H. Heisser et al., "Valveless microliter combustion for densely packed arrays of powerful soft actuators," *Proc. Nat. Acad. Sci.*, vol. 118, no. 39, Sep. 2021, Art. no. 2642, doi: 10.1073/pnas.2106553118.

[21] S. S. Robinson et al., "Integrated soft sensors and elastomeric actuators for tactile machines with kinesthetic sense," *Extreme Mech. Lett.*, vol. 5, pp. 47–53, Dec. 2015, doi: 10.1016/j.eml.2015.09.005.

[22] C. H. King et al., "Fabrication and characterization of a balloon actuator array for haptic feedback in robotic surgery," *J. Med. Devices*, vol. 2, no. 4, Dec. 2008, Art. no. 23652, doi: 10.1115/1.2996593.

[23] X. Wu, H. Zhu, S. - H. Kim, and M. G. Allen, "A portable pneumatically actuated refreshable braille cell," in *Proc. IEEE Int. Solid-State Sensors, Actuators Microsystems Conf.*, 2007, pp. 1409–1412, doi: 10.1109/SENSOR.2007.4300407.

[24] X. Wu, S. H. Kim, H. Zhu, and M. G. Allen, "A refreshable braille cell based on pneumatic microbubble actuators," *IEEE/ASME J. Microelectromech. Syst.*, vol. 21, no. 4, pp. 908–916, Aug. 2012, doi: 908-91610.1109/JMEMS.2012.2190043.

[25] A. Russomanno, R. B. Gillespie, S. O'Modhrain, and J. Barber, "A tactile display using pneumatic membrane actuators," in *Proc. Eurohaptics*, 2014, pp. 445–447.

[26] Microfluidic Skin, "HaptX: Haptic gloves for virtual reality and robotics." 2019. Accessed: Nov. 20, 2022. [Online]. Available: https://haptx.com/technology/

[27] N. Besse, S. Rosset, J. J. Zarate, and H. Shea, "Flexible active skin: Large reconfigurable arrays of individually addressed shape memory polymer actuators," *Adv. Mater. Technol.*, vol. 2, no. 10, Aug. 2017, Art. no. 1700102, doi: 10.1002/admt.201700102.

[28] S. Biswas and Y. Visell, "Emerging material technologies for haptics," *Adv. Mater. Technol.*, vol. 4, no. 4, Mar. 2019, Art. no. 1900042, doi: 10.1002/admt.201900042.

[29] C. C. Unger et al., "Data for all: Monolithic microfabricated valves and pumps by multilayer soft lithography," *Science*, vol. 288, no. 5463, pp. 113–116, Apr. 2000, doi: 10.1126/science.288.5463.113.

[30] C. Glick et al., "Rapid assembly of multilayer microfluidic structures via 3D-printed transfer molding and bonding," *Microsystems Nanoeng.*, vol. 2, Nov. 2016, Art. no. 16063, doi: 10.1038/micronano.2016.63.

[31] M. Zhu, S. Biswas, S. I. Dinulescu, N. Kastor, E. W. Hawkes, and Y. Visell, "Soft, wearable robotics and haptics: Technologies, trends, and emerging applications," *Proc. IEEE*, vol. 110, no. 2, pp. 246–272, Feb. 2022, doi: 10.1109/JPROC.2021.3140049.

[32] D. Fuard, T. Tzvetkova-Chevolleau, S. Decossas, P. Tracqui, and P. Schiavone, “Optimization of poly-di-methyl-siloxane (PDMS) substrates for studying cellular adhesion and motility,” *Microelectron Eng.*, vol. 85, no. 5, pp. 1289–1293, May/Jun. 2008, doi: 10.1016/j.mee.2008.02.004.
[33] L. Marechal, P. Balland, L. Lindenroth, F. Petrou, C. Kontovounisios, and F. Bello, “Toward a common framework and database of materials for soft robotics,” *Soft Robot.*, vol. 8, no. 3, pp. 284–297, Jun. 2021, doi: 10.1089/soro.2019.0115.
[34] L. A. Jones and H. Z. Tan, “Application of psychophysical techniques to haptic research,” *IEEE Trans. Haptics*, vol. 6, no. 3, pp. 268–284, Jul.–Sep. 2013, doi: 10.1109/TOH.2012.74.

Boxue Shan received the M.E. degree in biomedical engineering from Beihang University, Beijing, China, in 2021, where he is currently working toward the Ph.D. degree in mechanical engineering. His research interests include haptic device, human-machine interaction, VR, and robotics.

Congying Liu received the B.S. degree in mechanical engineering from Tongji University, Shanghai, China, in 2021. He is currently working toward the master’s degree in mechanical engineering with Beihang University, Beijing, China. His research interests include haptic device, haptic rendering, and haptic human-machine interface.

Yuan Guo received the M.E. degree in mechanical engineering from Chongqing Jiaotong University, Chongqing, China, in 2015. He is currently working toward the Ph.D. degree in mechanical engineering with Beihang University, Beijing, China. His research interests include haptics, human-machine interaction, force feedback glove, VR, and robotics.

Yiheng Wang received the B.S. degree in mathematics and applied mathematics from Beihang University, Beijing, China, in 2022. She is currently working toward the master’s degree in systems engineering with Beihang University. Her research interests include haptic device, human-machine interaction, and robotics.

Weidong Guo received the Ph.D. degree in mechanical engineering from Beihang University, Beijing, China, in 1995. He is currently a Professor with the Robotics Institute, Beihang University. His research interests include robotic dexterous hand, haptic human-machine interface, medical robotic system, and virtual prototyping technology.

Yuru Zhang (Senior Member, IEEE) received the Ph.D. degree in mechanical engineering from Beihang University, Beijing, China, in 1987. Her research interests include haptic human-machine interface, medical robotic systems, robotic dexterous manipulation, and virtual prototyping. She is an Associate Editor for IEEE ROBOTICS AND AUTOMATION LETTERS.

Dangxiao Wang (Senior Member, IEEE) received the Ph.D. degree in mechanical engineering from Beihang University, Beijing, China, in 2004. He is currently a Professor and the Deputy Director of the State Key Laboratory of Virtual Reality Technology and Systems, Beihang University. His research interests include haptic device, haptic rendering, and medical robotic systems. From 2014 to 2017, he was the Chair of Executive Committee of the IEEE Technical Committee on Haptics.